Secondary aerosol formation under a special dust transport event: impacts from unusually enhanced ozone and dust backflows over the ocean

Da Lu[1], Hao Li[1], Guochen Wang[1], Xiaofei Qin[1], Na Zhao[1], Juntao Huo[2], Fan Yang[3], Yanfen Lin[2], Jia Chen[2], Qingyan Fu[2], Yusen Duan[2], Xinyi Dong[4], Congrui Deng[1], Sabur F. Abdullaev[5], Kan Huang[1,6*]

[1]Center for Atmospheric Chemistry Study, Shanghai Key Laboratory of Atmospheric Particle Pollution and Prevention (LAP[3]), National Observations and Research Station for Wetland Ecosystems of the Yangtze Estuary, Department of Environmental Science and Engineering, Fudan University, Shanghai, 200433, China

[2]State Ecologic Environmental Scientific Observation and Research Station for Dianshan Lake, Shanghai Environmental Monitoring Center, Shanghai, 200030, China

[3]Pudong New District Environmental Monitoring Station, Shanghai 200122, China

[4]School of Atmospheric Sciences, Nanjing University, Nanjing 210023, China

[5]Physical Technical Institute of the Academy of Sciences of Tajikistan, Dushanbe, Tajikistan

[6]Institute of Eco-Chongming (IEC), Shanghai, 202162, China

Corresponding author: huangkan@fudan.edu.cn

Abstract

In the autumn of 2019, a five-day long-lasting dust event was observed using a synergy of field measurement techniques in Shanghai. This particular dust event stood

out from others due to its unique characteristics, including low wind speed, high relative humidity, elevated levels of gaseous precursors, and contrasting wind patterns at different altitudes. During this event, three distinct dust stages were identified. The first stage was a typical dust invasion characterized by with high concentrations of particulate matters but relatively short duration. In contrast, the second stage exhibited an unusual enhancement of ozone, attributed to compound causes of weak synoptic system, transport from the ocean, and subsidence of high-altitude ozone down drafted by dust. Consequently, gas phase oxidation served as the major formation pathway of sulfate and nitrate. In the third stage of dust, a noteworthy phenomenon known as dust backflow occurred. The dust plume originated from the Shandong Peninsula and slowly drifted over the Yellow Sea and the East China Sea before eventually returning to Shanghai. Evidence of this backflow was found through the enrichment of marine vessel emissions (V and Ni) and increased solubility of calcium. Under the influence of humid oceanic breezes, the formation of nitrate was dominated by aqueous processing. Additionally, part of nitrate and sulfate were directly transported via sea salts, evidenced by their co-variation with Na^+ and confirmed through thermodynamic modeling. The uptake of NH_3 on particles, influenced by the contributions of alkali metal ions and aerosol pH, regulated the formation potential of secondary aerosol. By developing an upstream-receptor relationship method, the amounts of transported and secondarily formed aerosol species were separated. This study highlights that the transport pathway of dust, coupled with environmental conditions, can significantly modify the aerosol properties, especially at the complex land-sea interface.

1. Introduction

Dust serves as a significant natural source of aerosols, constituting approximately half of the tropospheric aerosols (Zheng et al., 2016). Dust aerosols play crucial roles in environmental and climatic changes by affecting the radiation balance (Feng et al., 2020; Nagashima et al., 2016; Goodman et al., 2019). The optical properties of dust aerosols are influenced by various parameters of iron oxides, including refractive indices, size distributions, and mineralogical compositions. Consequently, these factors introduce potential uncertainties regarding the role of dust in climate forcing (Zhang et al., 2015; Jeong, 2008). Furthermore, dust aerosols have important impacts on tropospheric chemistry by participating in heterogeneous and photolysis reactions in the atmosphere (Wang et al., 2014; Liu et al., 2018). During transport, dust can mix with gaseous pollutants, toxic metals, and soot, thereby affecting air quality immediately and potentially posing public health hazards (Liu et al., 2021; Wang et al., 2021). Moreover, Barkley et al. (2021) found that iron-containing aerosols transported from Africa to the equatorial North Atlantic Ocean provided plentiful nutrients to algae in the ocean and accumulated inside algae.

The irregular shapes of dust particles provide an efficient medium for heterogeneous reactions with NO_2, O_3, SO_2, and NH_3, thereby altering the particle size spectrum, hygroscopicity, and radiative properties (Hsu et al., 2014; Tian et al., 2021; Jiang et al., 2018). Jiang et al. (2018) observed a significant increase in nitrate and sulfate concentrations during a dust period in March 2010 in Shanghai. This elevation was attributed to the presence of moderate to high levels of relative humidity and gaseous precursors, implying that dust can efficiently promote the formation of sulfate and nitrate. Previous studies have revealed that HNO_3 formed through the reactions of NO_2 with hydroxyl radical or N_2O_5 hydrolysis preferentially reacts with mineral dust

particles and produce nitrate, which serves as the primary source of nitrate during dust episodes (Tang et al., 2016; Wu et al., 2020). Improvements in the simulation of sulfate were achieved by employing various parameterization schemes for the heterogeneous uptake of SO_2 on natural dust surfaces in the presence of NH_3 and NO_2 under different relative humidity conditions(Zhang et al., 2019). Wang et al. (2018) simulated that heterogeneous reactions on dust accounted for the majority of nitrate over the Yellow Sea and the East China Sea during the dust long-range transport. Tang et al. (2017) conducted a comprehensive review on the effect of dust heterogeneous reactions on the tropospheric oxidation capacity. They proposed that high RH (> 80%) and a wider range of temperature should be considered in the laboratory studies of heterogeneous reactions of mineral dust. Additionally, more comprehensive kinetic models should be developed to understand the complex multiphase reactions.

Controversies have arisen regarding the mixing of dust and anthropogenic aerosols. Zhang et al. (2005) found that anthropogenic aerosols separated with dust during a dust event in Qingdao, China. Coincidentally, a time-lag between dust and anthropogenic aerosols was observed in Japan and South Korea downstream of the dust transport. Single particle analysis revealed that sulfate in fine particles appeared 12 hours before the dust arrival in Japan. Wang et al. (2013) also observed a lag of 10 - 12 hours between dust and anthropogenic aerosols on a dust day in Shanghai (Wang et al., 2013). Furthermore, Huang et al. (2019) documented vertical differences in long-transported aerosols during a pollution event in Taiwan. Dust from the Gobi Desert in Inner Mongolia and China existed at the altitudes of 0.8km and 1.90km, respectively, while biomass burning aerosols from South Asia were present at higher altitudes of 3.5km.

Coastal regions often experience a mixture of inland anthropogenic emissions and

releases from the ocean, making regional pollution complex in these areas (Wang et al.; Hilario et al., 2020; Patel and Rastogi, 2020; Perez et al., 2016; Wang et al., 2017). The eastern coast of China， bordering the East China Sea and the Yellow Sea, is particularly influenced by the Asian monsoon and high emissions from inland industries, resulting in highly intricate meteorological and pollution conditions (Hilario et al., 2020). Furthermore, the marine boundary layer in this region exhibits significant seasonal and diurnal variations in , relative humidity and temperature further impacting photochemical processes and heterogeneous reactions on aerosol surfaces (Zhao et al., 2021). Sea and land breezes play a crucial role in this coastal area. During the night, land breezes carry pollutants from the land to the sea. Subsequently, during the day, these land breezes transform into sea breezes, bringing the pollutants back over the sea. This phenomenon leads to an increase in air pollutants over the land (Zhao et al., 2021). For instance, Wang et al. (2022b) found that during the ozone pollution in Shanghai in 2018, the presence of O_3 at high altitudes at night was transported vertically downward during the daytime and high O_3 over the ocean was transported horizontally to the land, jointly contributing to regional O_3 pollution in Shanghai. Also, one dust episode in 2014 was observed over Shanghai via detouring from northern China due to the blocked north Pacific subtropical high-pressure system (Wang et al., 2018).

Previous studies have shown that about 70% of Asian dust traverses the eastern coast of China before moving towards the Korean Peninsula, the Sea of Japan, and eventually reaching the Pacific Ocean. The eastern coast of China serves as a crucial route for Asian dust transport to the Pacific Ocean (Arimoto et al., 1997; Huang et al., 2010a). Most previous research has focused on typical dust events characterized by strong intensities, high wind speed, low humidity, and low oxidants (Li et al., 2017; Ma

et al., 2019; Xu et al., 2017; Xie et al., 2005). In contrast, this study aims to depict an atypical dust event was observed in Shanghai, a coastal mega-city in Eastern China. The unusualness of the meteorological conditions, transport pathways, and air pollutants during the particular dust event was explicitly described. The study involves categorizing the dust event into three stages and comparing the aerosol chemical compositions between these stages. By focusing on the second and third stages, the different formation mechanisms of nitrate and sulfate were investigated. The amounts of major aerosol species from transport and secondary formation were estimated based on a simplified method of relating the upstream and receptor simultaneous measurements.

2. Methodology

2.1. Observational sites

At Shanghai Pudong Environmental Monitoring Station (31°13′ N, 121°32′E), comprehensive measurements of various atmospheric parameters were conducted. All the instruments were installed on the top floor of a building, about 25m above the ground level. As shown in Figure S1, the sampling site is situated at the eastern tip of Shanghai, close to the coastal line. During November, the mean temperature and relative humidity in Shanghai were recorded as 17.3℃ and 72% respectively. In autumn and winter, air pollutants originating from upstream urban regions often undergo transport to Shanghai via high-pressure systems. Additionally, air pollutants in Shanghai tended to linger at the sea/land boundary regions due to the sea-land breeze (Shen et al., 2019).

In addition to the measurements taken in Shanghai, data from environmental monitoring stations in Qingdao and Lianyungang are also incorporated into this study.

2.2. Instrumentation

A set of online instruments was set up at the Pudong observational site. Inorganic ions (NO_3^-, SO_4^{2-}, Cl^-, Na^+, NH_4^+, K^+, Mg^{2+}, Ca^{2+}) in $PM_{2.5}$ and soluble gases (NH_3, HNO_3, HCl, HONO) were measured by an online ion chromatography (IC, MARGA-1S, Metrohm). It operated at a flow rate of 16.7 L/min with a time resolution of one hour. Briefly, air was drawn into a $PM_{2.5}$ cyclone inlet and passed through a wet rotating denuder (gases) and a steam jet aerosol collector (aerosols). Subsequently, the aqueous samples were analyzed with ion chromatography. More details can be found in (Xu et al., 2020). Hourly trace metals (Si, Ca, Cu, Fe, K, Co, Mn, Cr, Zn, Pb, As, Cd, V, Ni) in $PM_{2.5}$ were measured by using the Xact 625 multi-metals monitor (Cooper Environmental, Beaverton, OR, USA). Particles were collected onto a Teflon filter tape at a flow rate of 16.7 L/min, and then transported into the spectrometer where the particles were analyzed with an X-ray fluorescence. Organic carbon and elemental carbon were measured by an in situ Semi-Continuous Organic Carbon and Elemental Carbon aerosol analyzer (RT-4, Sunset Laboratory, Beaverton, Oregon, USA). The concentration of mineral aerosols is calculated by summing the major mineral elements with oxygen for their normal oxides, i.e., [Minerals]= (2.2*Al+2.49*Si+1.63*Ca+2.42*Fe+1.94*Ti) (Malm et al., 1994). The concentration of OM (organic matters) is estimated by multiplying OC with a factor of 2.

The concentrations of particles and gaseous pollutants were measured by a set of

Thermo Fisher Scientific instruments, including $PM_{2.5}$ (Thermo 5030i), PM_{10} (Thermo 5030i), SO_2 (Thermo Fisher 43i), NO_x (Thermo Fisher 42i), O_3 (Thermo Fisher 49i), and CO (Thermo Fisher 48i-TLE). Meteorological parameters (ambient temperature, relative humidity, wind speed, and wind direction) were obtained by a Vaisala Weather transmitter (WXT520). Other supplementary parameters such as the height of planetary boundary layer (PBL), vertical profiles of ozone and aerosol extinction were obtained by a ceilometer (CL31, Vaisala), ozone lidar (LIDAR-G-2000, WUXIZHONGKE), and aerosol lidar (AGJ, AIOFM), respectively.

2.3. Thermodynamic simulation of aerosol pH and aerosol liquid water content

The ISORROPIA II model is subject to the principle of minimizing the Gibbs energy of the multi-phase aerosol system, leading to a computationally intensive optimization problem (Song et al., 2018). ISORROPIA II calculates the aerosol pH, ALWC (aerosol liquid water content) and compositions of ammonia-sulfate-nitrate-chloride-sodium-calcium-potassium-magnesium in the thermodynamic equilibrium with gas-phase precursors. The performances and advantages of ISORROPIA over the usage of other thermodynamic equilibrium codes has been assessed in numerous studies (Nenes et al., 1998; West et al., 1999; Ansari and Pandis, 1999; Yu et al., 2005). The ISORROPIA running in the forward mode at the metastable state was applied in this study.

2.4. Hybrid Single-Particle Lagrangian Integrated Trajectory Model

The HYSPLIT (Hybrid Single-Particle Lagrangian Integrated Trajectory) was used to compute the backward trajectories of the air parcels during the dust events. In this study, the HYSPLIT model was driven by meteorological data outputs from the

Global Data Assimilation System (GDAS) (Su et al., 2015), which is available at ftp://arlftp.arlhq.noaa.gov/pub/archives/gdas1. Air mass trajectories were launched at different heights from the ground and a total duration of 48 hours simulation was conducted.

2.5. Calculation of uptake coefficient of NH_3 (γ_{NH3}) on particles

NH_3, being the most abundant alkaline species in the atmosphere, plays a crucial role in acid neutralization and secondary aerosol formation. To assess the gas-particle partitioning of NH_3, the uptake coefficient of NH_3 (γ_{NH3}) on particles is calculated as below. Initially, the quasi-first-order reaction rate constant for heterogeneous conversion from NH_3 to NH_4^+ (k_{het}, s^{-1}) is calculated according to (Liu et al., 2022).

$$k_{het} = \frac{2(C_{NH_4^+,t_2} - C_{NH_4^+,t_1})}{(C_{NH_3,t_2} + C_{NH_3,t_1})(t_2 - t_1)}$$

k_{het} is only valid when c_{NH4+} increases, while c_{NH3} decreases assuming a constant emission rate from t_1 to t_2 (1 h in this study). Then, the uptake coefficient of NH_3 (γ_{NH3}) on particles can be calculated as below (Liu et al., 2022; Wang and Lu, 2016).

$$\gamma_{NH_3} = \frac{4k_{het}}{S\omega} = \frac{4k_{het}}{S\sqrt{\frac{8RT}{\pi M}}}$$

where S is the surface area of particles ($m^2\ m^{-3}$) measured using SMPS and APS. ω is the velocity of NH_3 molecules. T is the ambient temperature (K). R is the ideal gas constant, and M is the molecular weight of NH_3 (kg mol^{-1}).

3. Results and Discussion

3.1. Characteristics of an unusual dust event

Figure 1 shows the time series of PM_{10}, $PM_{2.5}$, meteorological parameters, as well as the vertical profiles of aerosol extinction coefficient and depolarization ratio observed at the Shanghai sampling site from October 25 to November 6, 2019. From October 25 to 28, the mean wind speed remained relatively low of 0.9±0.72m/s with a peak value of 3.1m/s, and predominantly blowing from the northwest. The mean concentration of $PM_{2.5}$ and PM_{10} was 34.7 and 44.2 μg/m^3, respectively. Starting at 4:00 LST on October 29, the concentration of PM_{10} increased sharply and lasted till November 2 (Figure 1d). The aerosol lidar observation indicated that both the aerosol extinction coefficient and depolarization ratio extended from the ground to around 2km during the same period. Notably, the enhanced depolarization ratio (>0.1) suggested the occurrence of a prolonged dust event in Shanghai. Throughout the entire dust period, the mean concentrations of $PM_{2.5}$ and PM_{10} reached 53.3 ± 20.5μg/m^3 and 172.4 ± 70.2μg/m^3, respectively, yielding a low $PM_{2.5}/PM_{10}$ ratio of 0.34 ± 0.15. As a comparison, $PM_{2.5}$ and PM_{10} during the non-dust period was 38.9μg/m^3 and 49.8μg/m^3, respectively, exhibiting a relatively high $PM_{2.5}/PM_{10}$ ratio of 0.62 ± 0.20.

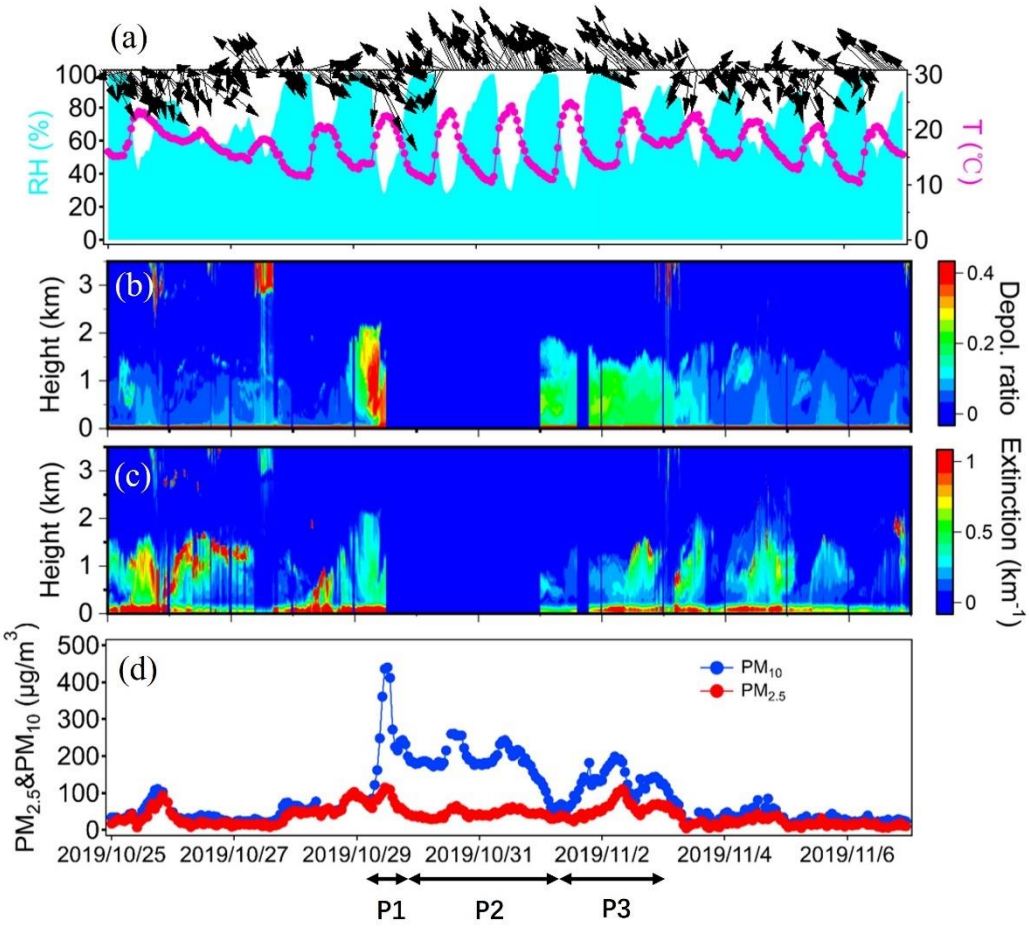

Figure 1. Time series of (a) relative humidity, temperature, wind vectors, (b) aerosol depolarization ratio, (c) aerosol extinction coefficient, (d) mass concentrations of $PM_{2.5}$ and PM_{10} during the study period. Three dust stages, i.e., P1, P2, and P3 are also marked. The missing aerosol lidar data were due to instrument malfunction.

The occurrences of dust are typically accompanied by low relative humidity and strong winds due to the passage of cold fronts (Huang et al., 2010b; Huang et al., 2010a; Wang et al., 2013; Wang et al., 2018). However, in this study, relative humidity was exceptionally high with the mean value of 71±26%. It showed strong diurnal variation, reaching its minimum in the daytime and even close to 100% in the nighttime (Figure 1a). Additionally, wind speed was low of 0.54±0.59m/s with a maximum of 2.6m/s. This stagnant synoptic condition led to elevated concentrations of main gaseous

pollutants such as O_3, SO_2, and NO_2, with mean values of 86.0±47.8μg/m^3, 11.8±3.4μg/m^3, and 63.3±27.9μg/m^3, respectively, even higher than those during the non-dust period.

We further divided the dust event into three stages based on the temporal characteristics of PM_{10} and the transport patterns of air masses. As shown in Figure 1d, PM_{10} quickly climbed from 4:00 on October 29 and reached a maximum of 436μg/m^3 after 8 hours. The air masses primarily originated from the semi-arid regions of northwest China (Figure 2d), which was consistent with both the near surface wind observation (Figure 1a) and wind lidar observation (Figure 2a). The wind profiles showed prevailing northwest winds from the surface up to around 2km before noon on October 29, indicating the presence of a strong synoptic system. Afterwards, PM_{10} quickly decreased to 199 μg/m^3 at 20:00, October 29 within 8 hours. This was primarily attributed to the shift of wind directions. As shown in Figure 2a, while winds above 700m continued to blow from the northwest, near- surface winds had shifted from the southeast. Due to Shanghai's coastal location adjacent to the East China Sea, the relatively clean southeasterlies diluted the local air pollutants, thereby explaining the quick decline in PM10 concentrations. This initial dust episode occurring from 4:00 - 13:00 on October 29 was defined as Stage P1.

Despite the persistent southeasterly winds, the dust event did not come to a complete halt. Even under these prevailing winds, hourly PM_{10} concentrations remained above 150 μg/m^3 until November 1, gradually decreasing to 65 μg/m^3 at 03:00, November 1 (Figure 1d). Compared to P1, wind speed during this stage was as low as 0.4 ± 0.5m/s, while RH was moderately high of 70 ± 26%. Although the daytime RH stayed low between 30% and 50%, it frequently soared above 90% at nighttime. Figure

2e shows that although the air masses originated from the Gobi Desert, they also traversed considerable coastal regions. The wind profiles further indicated that while northwest winds prevailed at altitudes higher than 500m, east and northeast winds were dominant below 500m (Figure 2b). Consequently, the relatively high RH during this period can be attributed to the mixing of dust plumes with coastal sea breezes. This dust episode from 14:00, October 29 to 3:00 on November 1 was designated as Stage P2.

Following P2, PM_{10} and $PM_{2.5}$ rose again and peaked at 5:00 and 9:00 on November 2 with the hourly concentration of 199 and 117μg/m^3, respectively. Different from P1 and P2, the air masses during this stage originated from the Shandong Peninsula and the northern region of Jiangsu province, and then migrated over the Yellow Sea and the East China Sea (Figure 2f). Typically, dust plumes tend to travel eastward, impacting the western Pacific region and even distant oceanic regions (Wang et al., 2018; Nagashima et al., 2016). However, in this case, the air masses evidently deviated and pushed the dust back towards the mainland. The wind profiles on November 2 revealed that winds within the detected altitude range predominantly originated from the eastern and southeastern oceanic regions (Figure 2c). This probably indicated the mixing between dust plumes and humid oceanic air masses was quite sufficient, which was also reflected by the highest average RH of 76 ± 24% among the three stages of the dust event. Moreover, the concentrations of O_3 and NO_2 at this stage were higher than those of P1 and P2, potentially promoting the formation of secondary aerosol components and will be discussed later. This rarely observed dust backflow transport episode from 4:00 on November 1 to 23:00 on November 2 was designated as Stage P3.

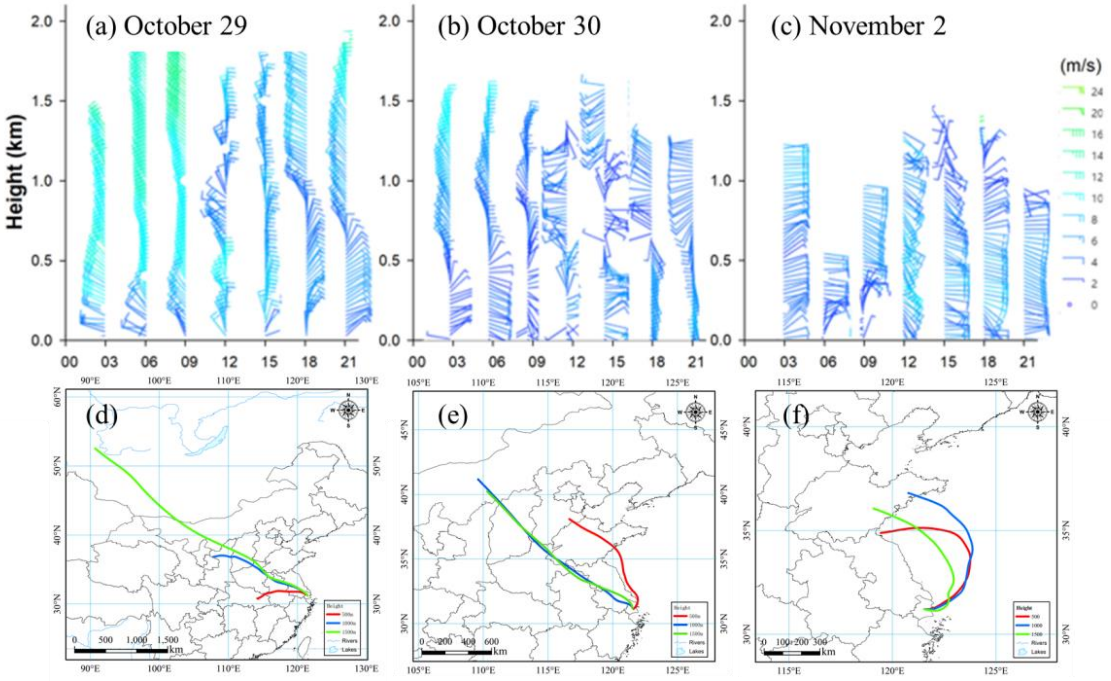

289

290 Figure 2. Wind profiles observed by a wind profiler radar on (a) October 29, (b) October
291 30, and (c) November 2. 48-hour backward trajectories simulated at the sampling site
292 starting from (d) 4:00 AM, October 29, (e) 9:00 AM, October 30, and (f) 13:00 PM,
293 November 2. The red, blue, and green trajectories represented starting altitudes of 100,
294 500, and 1500m, respectively.

295

296 **3.2. Comparisons of aerosol chemical compositions among the three dust stages**

297 Figure 3a shows the time-series of hourly aerosol chemical components,
298 including SNA (NO_3^-, SO_4^{2-}, and NH_4^+), OM, EC, and mineral aerosols in $PM_{2.5}$.
299 During P1, the mean concentration of SNA was 49.9 ± 31.6 μg/m^3. The mineral
300 aerosols reached 16.4 ± 14.6 μg/m^3, accounting for 19% in $PM_{2.5}$. The contribution of

OM to $PM_{2.5}$ was almost identical to that of mineral aerosols (Figure 3b).

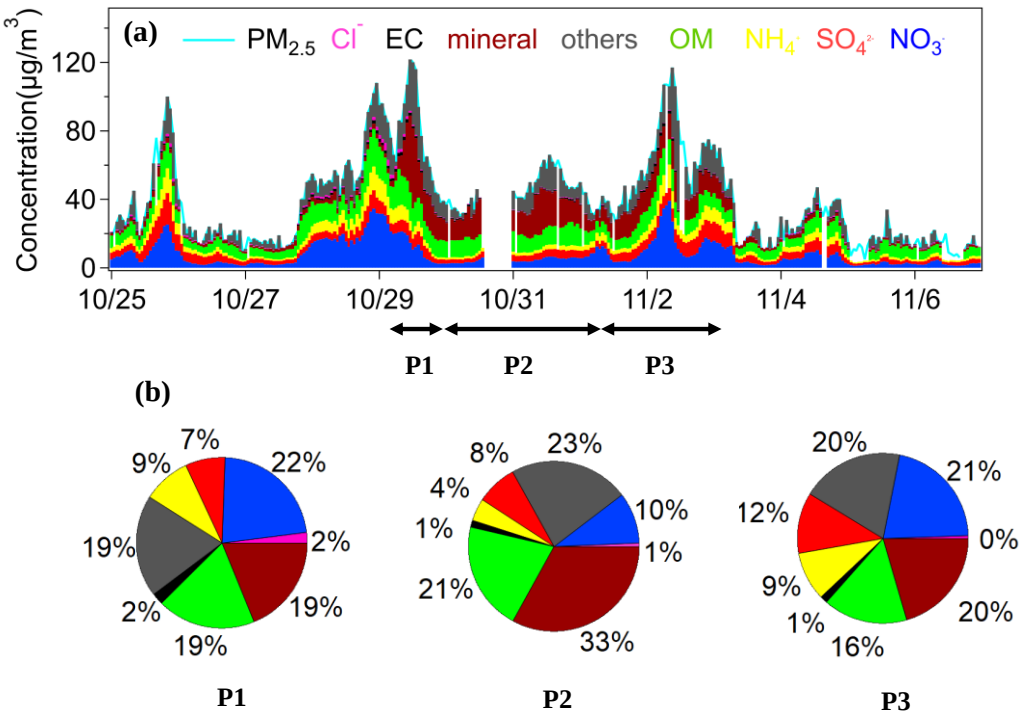

Figure 3. (a) Times-series of major chemical components in $PM_{2.5}$ during the study period. (b) The mean proportion of major chemical components in $PM_{2.5}$ during the three dust stages.

During P2, mineral aerosols increased to 23.4±54.1μg/m^3 and accounted for 33% in $PM_{2.5}$, representing the highest among all three stages (Figure 3b). Due to the continuous dilution effect of dust on local anthropogenic pollutants, the concentrations and proportions of SNA in $PM_{2.5}$ were the lowest during this stage. For instance, NO_3^- only accounted for 10% in $PM_{2.5}$, indicating a suppression of nitrate formation to some extent. The levels of OM didn't exhibit obvious changes and averaged 10.1±2.1μg/m^3, accounting for 21% in $PM_{2.5}$.

During P3, mineral aerosols averaged 11.9±2.7μg/m^3, ranking the lowest among all three stages. The proportion of mineral aerosols in $PM_{2.5}$ decreased to 20%,

suggesting the dust backflow from the ocean was less enriched in mineral components. Compared to P2, SNA showed significant increases and much stronger diurnal variations during P3. SO_4^{2-}, NO_3^-, and NH_4^+ averaged 6.7 ± 2.4, 12.4 ± 8.9, and 5.4 ± 2.7μg/m^3, respectively. As shown in Figure 3b, the contribution of nitrate to $PM_{2.5}$ increased to 21%, while that of sulfate rose to 12%, the highest among all three stages. The concentration of OM (9.3±3.2μg/m^3) and its proportion (16%) during P3 were lower than the other two stages, likely due to the unconventional dust backflow transport pathway.

3.3. Unconventional features of the dust episodes

3.3.1. Unusually enhanced O_3 during dust

Figure 4 shows the hourly near surface ozone concentrations and vertical profiles of ozone during the study period. Interestingly, a few high O_3 peaks occurred during the dust event (Figure 4a). O_3 averaged 92.8 ± 52.8μg/m^3 during the dust, about 50% higher than the non-dust days. Among the three dust stages, O_3 substantially increased from 35.9 ± 36.4μg/m^3 during P1 to 80.7 ± 41.2μg/m^3 during P2, and further rose to 104.0 ± 48.7μg/m^3 during P3. The low O_3 during P1 can be attributed to the cleansing effect of the strong dust associated with the cold front, which was consistent with previous studies that reported reduced oxidant concentrations during intense dust events (Benas et al., 2013). Regarding the relatively high O_3 during P2 and P3, several causes may contribute to this phenomenon. Firstly, the mean wind speed was low of 0.4 and 0.6 m/s during P2 and P3, respectively. Consequently, this weak synoptic system exerted a weak dilution effect on the local air pollutants. A numerical study conducted during a similar period suggested that the reduction of boundary layer

height and the warming of the lower atmosphere accelerated the ozone formation by ~1 ppbv/h (Wang et al., 2020). Secondly, since the dust plume travelled mostly over the coastal and oceanic areas, a portion of O_3 could be transported from the high ozone oceanic areas (Wang et al., 2022b). Thirdly, the ozone lidar also detected high O_3 stripes during P2 and P3. As shown in Figure 5b, the high O_3 profiles extended from the surface to around 1km and the profile structure was similar to that of aerosol depolarization ratio. The subsidence of dust particles likely contributed to downward transport of high-altitude O_3, thereby influencing the elevated O_3 near the ground (Yang et al., 2022).

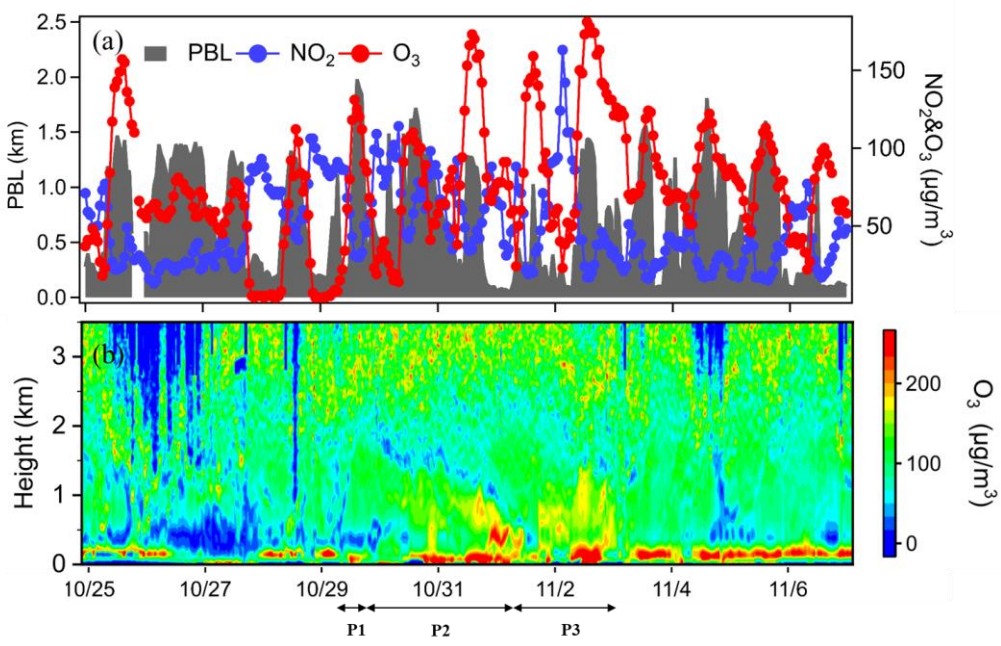

Figure 4. (a) Time-series of near surface O_3, NO_2 and planetary boundary layer height (b) Vertical profiles of ozone observed by the ozone Lidar.

3.3.2. Dust backflows during P3

The dust during P3 was diagnosed as a backflow transport pathway from the mainland to Shanghai through the Yellow Sea and the East China Sea, as determined by the backward trajectory analysis (Figure 2f). This unconventional dust transport

route, termed “dust backflow”, was consistent with a similar occurrence in 2014 when dust from northern China detoured over Shanghai (Wang et al., 2018). In this section, we have provided further evidences of the dust backflow from various aspects.

Figure 2f illustrates that the dust drifted away from the Shandong Peninsula, thus we selected two coastal sites in Shandong province for supplementary analysis. Figure S2 compares the time-series of hourly air pollutants at Qingdao, Lianyungang, and Shanghai. At Qingdao and Lianyungang, high PM_{10} concentrations were observed during October 30 – 31, indicating the invasion of dust in these regions. After about two days, PM_{10} peaked in Shanghai on early November 2. This temporal consistency aligned with the simulation duration of the backward trajectories, which lasted around 48 hours (Figure 2f). In Figure 9, it can be observed that in the upstream dust regions (i.e., Qingdao and Lianyungang), PM_{10} varied negatively with NO_2 and CO (the highlighted period in the figure). While in Shanghai, positive correlations between PM_{10} and both NO_2 (R^2=0.32) and CO (R^2=0.55) indicated that the dust during P3 served as a carrier for gaseous pollutants rather than acting a diluter.

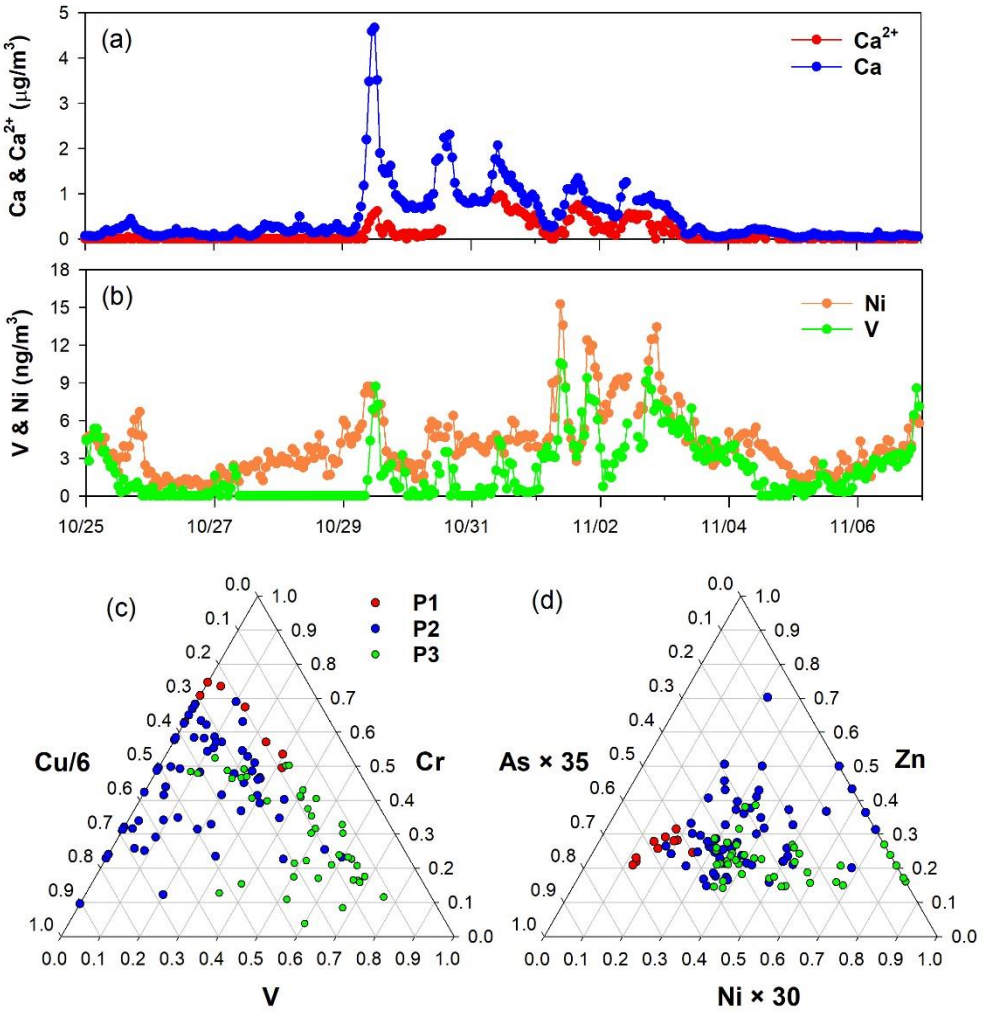

375

376 Figure 5. Time-series of (a) Ca, Ca^{2+}, (b) V, and Ni during the study period. (c)
377 Cu-Cr-V ternary diagram and (d) As-Zn-Ni ternary diagram among the P1 – P3 dust
378 episodes. Due to substantial concentration differences of various elements, some
379 elements are artificially changed to make most scatters appear around the centroid.

380

381 Additional evidence of dust backflows was provided from the perspective of
382 aerosol chemical tracers. Figure 5a plots the time-series of Ca and Ca^{2+}, representing
383 the total calcium and the soluble part of calcium, respectively. It was observed that Ca
384 and Ca^{2+} didn't exhibit a proportional variation trend, which should be related to the

385 solubility of calcium during different dust stages. During P1, the mean concentration of
386 Ca reached the highest of 1.63 ± 1.53μg/m^3 while Ca^{2+} was the lowest of 0.21 ±
387 0.20μg/m^3, thus resulting in the lowest Ca^{2+}/Ca ratio of 0.10 ± 0.08. As discussed in
388 Section 3.1, dust during P1 was the strongest and thus it contained higher fractions of
389 minerals, primarily in the form of insoluble metal oxides. The average concentrations
390 of Ca^{2+} and Ca during P2 were 0.33 ± 0.28μg/m^3 and 1.11 ± 0.46μg/m^3, respectively,
391 resulting in the higher Ca^{2+}/Ca ratio of 0.27 ± 0.20. As a comparison, the average
392 concentrations of $Ca^{2+}$and Ca during P3 reached 0.34 ± 0.20μg/m^3 and 0.78 ±
393 0.27μg/m^3, respectively, yielding the highest Ca^{2+}/Ca ratio of 0.38 ± 0.19. The
394 significantly higher solubility of calcium during P3 should be directly related to the
395 prolonged presence of dust plumes over the open ocean. The abundant water vapor over
396 the ocean could accelerate the dissolution of the insoluble components in particles
397 during the mixing between continental dust and oceanic air masses. Additionally, the
398 backflow transport pathway facilitated the entrainment of sea salts and contributed to
399 the increase of soluble calcium.

400 Figure 5b provides additional insights by displaying the time-series of V and Ni,
401 which are typical tracers of oil combustions (Becagli et al., 2012). They varied
402 significantly during the study period, and the mass concentrations of V and Ni increased
403 4 and 1.8 times during P3 compared to P2, respectively. Consistently, the enrichment
404 factors of Ni and V displayed higher values during P3 than P1 and P2 (Figure S3). The
405 trends are substantiated in the ternary diagrams, which are commonly applied to
406 illustrate the relative abundances of three components and infer the source variations
407 (Bozlaker et al., 2019; Cwiertny et al., 2008; Laskin et al., 2005). As shown in the Cu-
408 Cr-V ternary diagram (Figure 5c), the dust samples during P1 were positioned away

409 from the V-apex. As a comparison, the dust samples during P2 exhibited greater
410 scattering, manifesting enhanced anthropogenic contributions, e.g., from chrome
411 plating industries (Hammond et al., 2008). Compared to P2, the dust samples during P3
412 moved toward the V-apex, indicating a higher contribution from oil combustions
413 (Becagli et al., 2012). A similar pattern was observed in the As-Zn-Ni ternary diagram
414 (Figure 5d). The majority of dust samples during P2 spanned across the diagram,
415 reflecting contributions from mixed anthropogenic sources. Reciprocally, P3 was closer
416 to the Ni-apex. These lines of evidences collectively confirmed that the dust had mixed
417 with pollutants from marine vessel emissions over one of the busiest international
418 shipping trade routes (Fan et al., 2016) and was subsequently transported back to
419 Shanghai.
420
421 **3.4. Formation of secondary aerosols during the dust long-range transport**
422 **3.4.1. Comparison of typical chemical tracers**

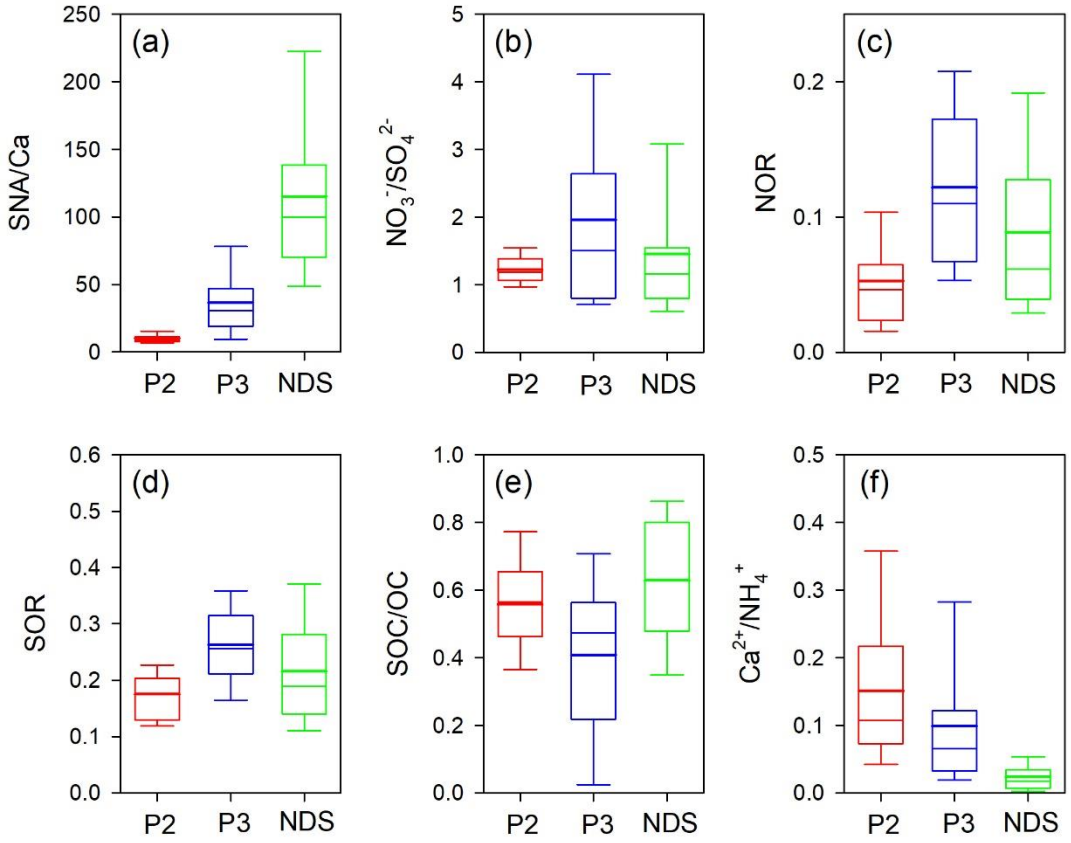

Figure 6. Box plots of (a) SNA/Ca, (b) NO_3^-/SO_4^{2-}, (c) NOR, (d) SOR, (e) SOC/OC, and (f) Ca^{2+}/NH_4^+ during P2, P3, and NDS, respectively.

To delve deeper into the formation characteristics of secondary aerosols in different stages, a variety of chemical tracers was investigated. The P1 dust stage was excluded from statistical analysis due to its short duration and limited data availability. Figure 6a shows the comparison of SNA/Ca ratios during P2, P3 and non-dust days (NDS). The SNA/Ca ratio can be used to assess the relative changes between secondary production and primary dust emission by eliminating the impact of meteorological conditions among different periods (Zheng et al., 2015). Compared to the two dust episodes, the SNA/Ca ratio is significantly higher during NDS. This can be attributed to the much lower concentrations of mineral aerosols during NDS, thus resulting in the

436 higher SNA relative to Ca. In terms of comparing P2 and P3, the average SNA/Ca ratio
437 during P3 was 3 times that of P2, indicating that the formation of secondary inorganic
438 aerosols was more prominent during the dust backflow. Regarding the NO_3^-/SO_4^{2-} ratios
439 (Figure 6b), they were close between NDS and P2, with NO_3^- slightly exceeding SO_4^{2-}.
440 The range of NO_3^-/SO_4^{2-} was the largest during P3 with a mean value of around 2,
441 suggesting that the dust backflow was more conducive to the accumulation of nitrate.
442 The nitrogen oxidation ratio ($NOR = NO_3^-/(NO_3^- + NO_2)$) and the sulfur oxidation ratio
443 ($SOR = SO_4^{2-}/(SO_4^{2-} + SO_2)$) were further used to gauge the extent of nitrate and sulfate
444 formation, both showing trends of P3>NDS>P2 (Figure 6c & 6d). It should be noted
445 that NOR and SOR cannot be used to realistically characterize the extent of nitrogen
446 and sulfur oxidation during transport-dominated pollution cases, as upstream aging
447 aerosols can significantly increase the above ratios (Ji et al., 2018). In the following
448 discussion, we will focus on the formation mechanism of SNA during different dust
449 stages.

450 The results of SOC/OC ratios differed from the above analysis that SOC/OC was
451 lower during P3 than during P2 and NDS (Figure 6e), suggesting that the formation of
452 secondary organic aerosols was not favored via the dust backflow. This may be due to
453 its maritime transport pathway as the emission intensity of volatile organic compounds
454 from the ocean is much lower than that from land sources. Consequently, the lacking of
455 organic aerosol precursors could be the main cause for the lower SOC/OC ratios during
456 P3. Finally, the Ca^{2+}/NH_4^+ ratio was employed to assess the relative contributions of
457 alkaline chemical components (Figure 6f). As expected, this ratio during the two dust
458 stages was much higher than that of NDS, indicating the important contribution of dust
459 to alkaline metal ions. The Ca^{2+}/NH_4^+ ratio was higher during P3 (0.15) than during P2

(0.10), which aligned with the findings presented in Section 3.2.

3.4.2. Distinct formation processes of secondary aerosols between P2 and P3

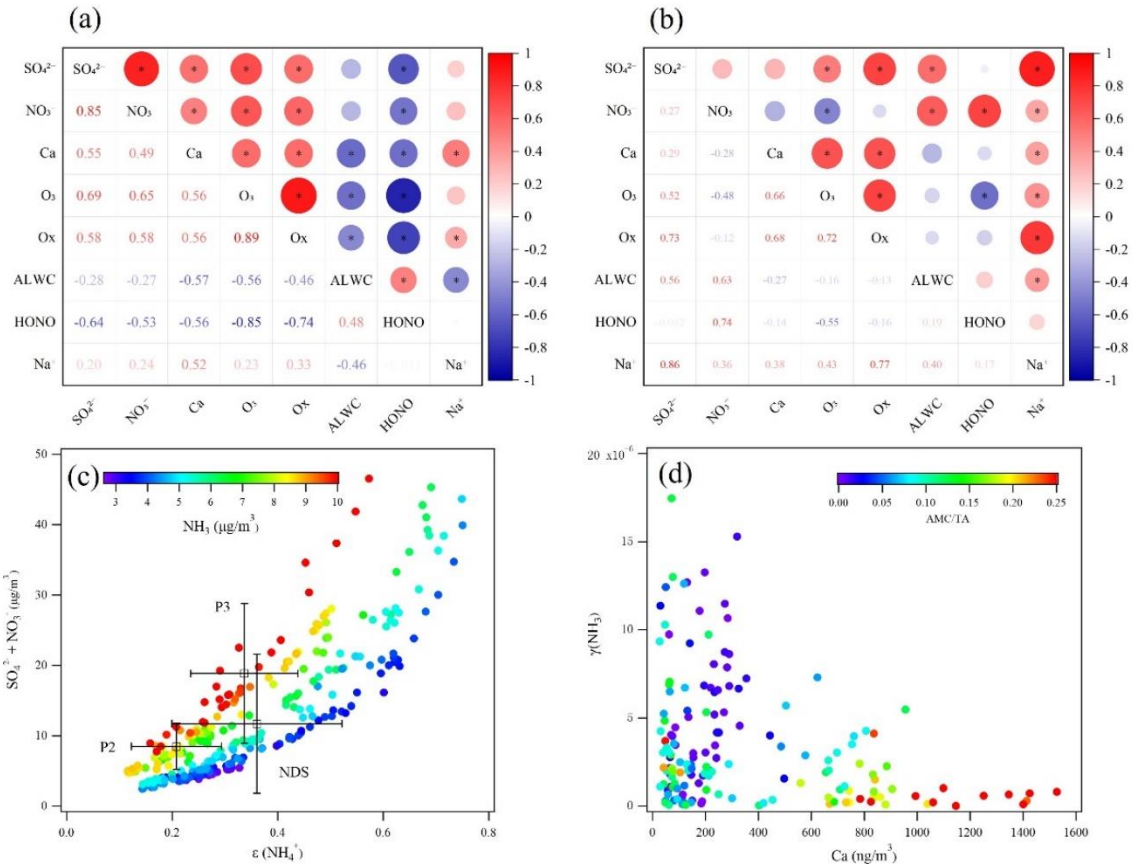

Figure 7. Correlation heatmaps during (a) P2 and (b) P3. (c) The mass concentrations of SO_4^{2-} and NO_3^- as a function of $\varepsilon(NH_4^+)$, with dots colored by the concentration of NH_3. (d) The uptake coefficient of NH_3 (γ_{NH3}) on particles as a function of Ca, with dots colored by the AMC/TA molar ratios. AMC and TA denote the total molar concentrations of Na^+, K^+, Mg^{2+}, and Ca^{2+} and the total molar concentrations of anions, respectively.

In this section, we further analyze the formation mechanism and key influencing factors of secondary components during P2 and P3. Figure 7a & 7b compare the

correlation heatmaps of SO_4^{2-} and NO_3^- with various parameters. During P2, both SO_4^{2-} and NO_3^- displayed the most significant correlations with O_3 and Ox (O_3+NO_2), while even negatively correlated with ALWC. In regard of the obvious ozone enhancement phenomenon as discussed in Section 3.3.1, photochemistry should be the main pathway for the secondary aerosol formation rather than the liquid phase processing. In addition, SO_4^{2-} and NO_3^- also showed moderate correlations with elemental Ca, suggesting that dust acted as a carrier to transport these salts, which can be derived from background minerals in dust (Wu et al., 2022) and dust heterogeneous reactions during the transport (Huang et al., 2010a).

As for P3, it showed a distinctly different correlation heatmap from P2. While SO_4^{2-} still demonstrates a correlation with O3, the relationship between NO_3^- and O_3 (as well as Ox) disappeared. On the contrary, both SO_4^{2-} and NO_3^- show significant correlations with ALWC. During P3, the average RH reached 76%, providing favorable conditions for liquid-phase reactions. Furthermore, by relating NO_3^- and the multiplication of ALWC and NO_2, the correlation coefficient (R^2 = 0.41) was further improved (Figure S4a). Similar results were observed by relating NO_3^- to the multiplication of ALWC and NO_2*O_3*NO_2 (a proxy of N_2O_5, (Huang et al., 2021)) (Figure S4b), confirming the dominant reaction pathway of nitrogen oxides to nitrate via the aqueous phase reactions. As a result, NO_3^- was also strongly correlated with HONO (Figure S4c), typically deriving from the heterogeneous reactions of NO_2 on the surface of moist particles (Alicke et al. (2002).

In addition, unlike P2, both SO_4^{2-} and NO_3^- showed moderate to significant correlations with Na^+. Since neither SO_4^{2-} nor NO_3^- correlated with Ca, it can be inferred that sea salts played a more important role in the transport of air pollutant during the

dust backflow over the ocean. To assess whether dust or sea salts participated in the heterogeneous reactions of secondary aerosol during P3, the ISORROPIA II model was run with different scenarios. Figure S5 shows the model performance for SO_4^{2-}, NO_3^-, NH_4^+, and NH_3 based on the SO_4^{2-}–NO_3^-–NH_4^+–Cl^-–NH_3–HCl–HNO_3 system. After adding Ca^{2+} into this thermodynamic equilibrium system, the correlations between the simulations vs observations for all four species were lowered with different extents (Figure S6). If Na^+ was added into the thermodynamic equilibrium system. the model performance was slightly improved (Figure S7). This corroborated that the heterogeneous reactions on dust were very limited while sea salts were intensively involved in the formation of secondary inorganic aerosols during the dust backflow.

To further explore the influencing factors affecting the formation of secondary inorganic aerosols, we examined the role of NH_3 in different stages, representing by the relationship between the gas-particle partitioning of ammonia ($\varepsilon(NH_4^+)$, defined as the ratio between particle phase ammonia (NH_4^+) and total ammonia (NH_x = NH_3+NH_4^+)) and the total acids (SO_4^{2-} + NO_3^-). As shown in Figure 7c, it is obvious that the total acids strongly co-varied with $\varepsilon(NH_4^+)$. Higher $\varepsilon(NH_4^+)$ resulted in higher concentrations of secondary aerosols. Moreover, under similar $\varepsilon(NH_4^+)$ conditions, higher NH_3 promoted stronger formation of secondary aerosols. Thus, both NH_3 and $\varepsilon(NH_4^+)$ collectively determined the aerosol formation potential. The mean states of P2, P3, and NDS are compared in Figure 7c. P2 had the lowest $\varepsilon(NH_4^+)$ with the mean value of 0.21, despite the relatively high concentrations of NH3 during this period (7.9 ± 1.0 μ g/m^3). The relatively low gas-particle partitioning of ammonia limited the neutralization of the acidic components. In contrast, NH_3 during P3 was the highest during the study period (9.8 ± 1.8 μg/m^3), and $\varepsilon(NH_4^+)$ (0.34) was only slightly lower

than that during NDS, thus effectively fostering the formation of secondary inorganic aerosols.

To explain this phenomenon, the uptake coefficient of NH_3 (γ_{NH3}) on particles, which is one of the important parameters affecting the gas-particle partitioning of ammonia, was calculated. Figure 7d shows the decreasing trend of γ_{NH3} with the increase of dust intensity (using Ca as an indicator). This coincided with a multi-year observational study in Beijing and Shijiazhuang, where γ_{NH3} obviously increased due to significant decline in alkali earth metal contents from the dust emission sources during 2018 – 2020 (Liu et al., 2022). Thus, this partially explained why $\varepsilon(NH_4^+)$ was relatively low during P2, which was ascribed to the reduced uptake capacity of NH_3 on particles.

The ion balance calculation indicated that the total anions and cations are in ideal equilibrium (Figure S8, regression slope = 0.99, R^2 = 0.99), indicating that both NH_4^+ and alkali metal cations (including Na^+, K^+, Mg^{2+}, and Ca^{2+}) contributed to the neutralization of acids to varying degrees. The ratio of alkali metal cations/total anions (AMC/TA) was used to color the data points in Figure 7d, showing an opposite trend between AMC/TA and γ_{NH3}. During P2, the mean value of AMC/TA reached 21%, implying that the neutralization of acids by NH_3 had been significantly suppressed, thus explaining `the decrease in the NH_3 uptake coefficient at high dust intensity. In contrast, the AMC/TA ratio decreased to 11% during P3, indicating a reduced competition between NH_3 and the alkali dust components. Finally, we also compared the aerosol pH at different stages, which was 3.2, 3.0, and 2.8 during P2, P3, and NDS, respectively. The relatively high aerosol acidity at P3 and NDS favored the uptake of alkaline gases (Liu et al., 2022), which also contributed to the higher (γ_{NH3}) at these two stages.

3.5. Estimation of transported and secondarily formed particles during P3

As discussed in previous sections, the aerosols observed during P3 could originate from both aged aerosols transported via the dust backflows and secondary formation. In this section, we aimed to estimate the contribution of transport and secondary formation to the main aerosol species, respectively, based on the simultaneous measurements at the Pudong site and the Lianyungang site. As discussed in Section 3.4.1, Lianyungang acted as an upstream region where dust drifted away from the mainland. The duration of dust observed at Lianyungang was approximately from 5:00 on October 30 to 16:00 on October 31, about 46 hours ahead of the dust invasion observed at Pudong (Figure S2).

To assess the extents of transported air pollutants, black carbon (BC) was used as a reference aerosol component. As shown in Figure S9, one BC pollution episode on October 30 at Lianyungang was observed. Correspondingly, another BC pollution episode emerged at Pudong on November 2after about 46 hours. Since the air mass trajectory from Lianyungang to Pudong predominantly traversed over the ocean, and considering that BC has no secondary sources, it can be reasonably assumed that the differences of BC concentrations between these two sites were ascribed to the removal processes of particles.

To determine the removal fractions of aerosols during dust transport, we first defined the average concentrations of various aerosol components during the preceding five hours of the dust at Pudong as their background concentrations. Then, a coefficient k was derived to calculate the removal fractions of aerosols during the dust transport as below.

$$k = \frac{AV_{LYG,BC} - (AV_{PD,BC} - BKG_{PD,BC})}{AV_{LYG,BC}}$$

$AV_{LYG,BC}$ and $AV_{PD,BC}$ represent the average concentration of BC at Lianyungang and Pudong during their respective dust period. $BKG_{PD,BC}$ represents the background concentration of BC at Pudong. Assuming that other aerosol species were removed with a similar efficiency as BC, the amounts of transported aerosol species from Lianyungang to Pudong can be estimated as below.

$$TP_{PD,i} = AV_{LYG,i} \times (1 - k)$$

$TP_{PD,i}$ represents the transported amounts of aerosol species *i*. Then, the secondarily formed aerosol species *i* at Pudong can be calculated as below.

$$SF_{PD,i} = AV_{PD,i} - BKG_{PD,i} - TP_{PD,i}$$

Figure 8 shows the results of the transported and the secondarily formed aerosol species during P3. It was calculated that the secondarily formed and transported NO_3^- averaged 6.8μg/m^3 and 4.7μg/m^3, accounting for about 45% and 31% of its total mass concentration, respectively. This was consistent with the earlier analysis that a considerable portion of nitrate was formed through the aqueous phase secondary formation. In contrast, it was calculated that the transported SO_4^{2-} accounted for about 42% of its total mass concentration, while the secondarily formed SO_4^{2-} was almost negligible. This was also consistent with the phenomenon that SO_4^{2-} correlated significantly with Na^+ (Figure 6b). As for NH_4^+, it exhibited a similar apportionment as NO_3^-, with the secondarily formed and transported NH_4^+ accounting for about 35% and 28% of its total mass concentration, respectively. Compared to NO_3^- and NH_4^+, OM was more dominated by transport (57%) while its secondary formation only accounted for about 13%.

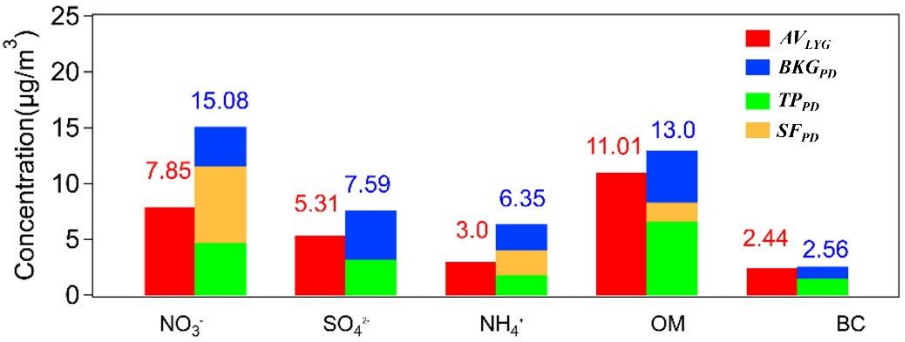

Figure 8. The apportioned concentrations of the major aerosol species during P3.

4. Conclusion

During October 29 to November 2, 2019, a long-lasting dust event was observed in Shanghai based on a synergy measurement of near surface air pollutants, aerosol lidar, wind profiling lidar, and air masses trajectory modeling. During the whole dust period, the mean concentrations of $PM_{2.5}$ and PM_{10} reached 53.3 ± 20.5μg/m^3 and 172.4 ± 70.2μg/m^3. Different from most dust events, this dust event was characterized of exceptionally high relative humidity (71 ± 26%) and low wind speed (0.54 ± 0.59m/s). Due to this stagnant synoptic condition, the mean concentrations of main gaseous pollutants such as O_3, SO_2, and NO_2 reached 86.0 ± 47.8μg/m^3, 11.8 ± 3.4μg/m^3, and 63.3 ± 27.9μg/m^3, respectively, even higher than those during the non-dust period.

The dust event was divided into three stages from P1 – P3. P1 was a short dust episode when wind profiles showed dominant northwest winds from the ground to the altitudes of around 2km, indicating the presence of a strong synoptic system. P2 was a dust episode when RH was moderately high of 70 ± 26% and the southeasterlies prevailed with partial air masses from coastal regions. P3 was a rarely observed dust

backflow transport episode. The air masses originated from the Shandong Peninsula and the northern region of Jiangsu province, and then migrated over the Yellow Sea and the East China Sea. RH reached the highest of 76 ± 24% among the three stages of the dust event.

During P2, mineral aerosols accounted for 33% in $PM_{2.5}$, the highest among all three stages. Abnormally high O_3 concentrations were observed, much higher than the non-dust days. This was partially due to the weak synoptic system that exerted weak dilution effect on the local air pollutants. The ozone lidar observed that the subsidence of dust particles probably down drafted high-altitude O_3 and also contributed to the high O_3 near the ground. As a result, sulfate and nitrate moderately correlated with O_3 while had almost no correlation with ALWC, indicating that the formation of secondary aerosols during P2 should be mainly promoted via the gas-phase oxidations.

During P3, a special phenomenon of dust backflow was observed and confirmed by various evidences. Two upstream sites (Qingdao and Lianyungang) showed dust occurrences about 48 hours ahead that of Shanghai, consistent with the transport duration of the dust backflow from the Shandong Peninsula to Shanghai over the Yellow Sea and the East China Sea. As a result, the highest Ca^{2+}/Ca ratio was observed due to that the lingerer of dust plumes over the open ocean. Moreover, contributions of V and Ni significantly increased, indicating the mixing between dust and marine vessel emissions. Different from P2, nitrate significantly correlated with ALWC but not with O_3, , indicating its aqueous-phase reaction pathway. Also, sulfate and nitrate exhibited moderate to strong correlations with Na^+, suggesting sea salts as a medium for the heterogeneous reactions.

By analyzing various chemical tracers, the formation extent of SNA was found

much stronger during P3 than during P2. Both NH_3 and $\varepsilon(NH_4^+)$ ($NH_4^+/(NH_3+NH_4^+)$) determined the concentrations of SNA. To explain the relatively high $\varepsilon(NH_4^+)$ values during P3, the uptake coefficient of NH_3 (γ_{NH3}) on particles is calculated. γ_{NH3} negatively varied with the intensity of dust, which were attributed to two factors. Higher contributions of alkali metal components suppressed the neutralization capacity of NH3 on acids, thereby lowering γ_{NH3} during P2. Also, relatively high aerosol pH during P2 didn't facilitate the uptake of NH3 and the subsequent aerosol formation.

Based on a simplified method, the amounts of transported and secondarily formed particles during P3 were quantified. It was calculated that about 45% and 31% of NO_3^- was contributed by secondary formation and transport, respectively. In contrast, the transported SO_4^{2-} accounted for about 42% of its total mass concentration while the rest was from its background concentration with negligible secondary formation. OM was dominated by transport (57%) while its secondary formation only accounted for about 13%.

Data Availability Statement

All data used in this study can be requested upon the corresponding author (huangkan@fudan.edu.cn).

Author contributions

KH, QF, and YD designed this study. JH, FY, YL, and JC performed data collection. DL and KH performed data analysis and wrote the paper. All have commented on and reviewed the paper.

Competing interests

The authors declare that they have no conflict of interest.

Acknowledgments

This work was financially supported by the National Science Foundation of China (42175119).

References

Alicke, B., Platt, U., and Stutz, J.: Impact of nitrous acid photolysis on the total hydroxyl radical budget during the Limitation of Oxidant Production/Pianura Padana Produzione di Ozono study in Milan, J. Geophys. Res.-Atmos., 107, 18, 10.1029/2000jd000075, 2002.

Ansari, A. S. and Pandis, S. N.: An analysis of four models predicting the partitioning of semivolatile inorganic aerosol components, Aerosol Science And Technology, 31, 129-153, 10.1080/027868299304200, 1999.

Arimoto, R., Ray, B. J., Lewis, N. F., Tomza, U., and Duce, R. A.: Mass-particle size distributions of atmospheric dust and the dry deposition of dust to the remote ocean, J. Geophys. Res.-Atmos., 102, 15867-15874, 10.1029/97jd00796, 1997.

Barkley, A., Olson, N., Prospero, J., Gatineau, A., Panechou, K., Maynard, N., Blackwelder, P., China, S., Ault, A., and Gaston, C.: Atmospheric Transport of North African Dust‐Bearing Supermicron Freshwater Diatoms to South America: Implications for Iron Transport to the Equatorial North Atlantic Ocean, Geophysical Research Letters, 48, 10.1029/2020GL090476, 2021.

Becagli, S., Sferlazzo, D. M., Pace, G., di Sarra, A., Bommarito, C., Calzolai, G., Ghedini, C., Lucarelli, F., Meloni, D., Monteleone, F., Severi, M., Traversi, R., and Udisti, R.: Evidence for heavy fuel oil combustion aerosols from chemical analyses at the island of Lampedusa: a possible large role of ships emissions in the Mediterranean, Atmos. Chem. Phys., 12, 3479-3492, 10.5194/acp-12-3479-2012, 2012.

Benas, N., Mourtzanou, E., Kouvarakis, G., Bais, A., Mihalopoulos, N., and Vardavas, I.: Surface ozone photolysis rate trends in the Eastern Mediterranean: Modeling the effects of aerosols and total column ozone based on Terra MODIS data, Atmospheric Environment, 74, 1-9, 10.1016/j.atmosenv.2013.03.019, 2013.

Bernard, F., Cazaunau, M., Grosselin, B., Zhou, B., Zheng, J., Liang, P., Zhang, Y., Ye, X., Daële, V., Mu, Y., Zhang, R., Chen, J., and Mellouki, A.: Measurements of nitrous acid (HONO) in urban area of Shanghai, China, Environmental Science and Pollution Research, 23, 5818-5829, 10.1007/s11356-015-5797-4, 2016.

Bozlaker, A., Prospero, J. M., Price, J., and Chellam, S.: Identifying and Quantifying the Impacts of Advected North African Dust on the Concentration and Composition of Airborne Fine Particulate Matter in Houston and Galveston, Texas, J Geophys Res-Atmos, 124, 12282-12300, 10.1029/2019jd030792, 2019.

Cwiertny, D. M., Baltrusaitis, J., Hunter, G. J., Laskin, A., Scherer, M. M., and Grassian, V. H.: Characterization and acid-mobilization study of iron-containing mineral dust source materials, J Geophys Res-Atmos, 113, Artn D05202

10.1029/2007jd009332, 2008.

Dall'Osto, M., Harrison, R. M., Coe, H., and Williams, P.: Real-time secondary aerosol formation during a fog event in London, Atmospheric Chemistry And Physics, 9, 2459-2469, 10.5194/acp-9-2459-2009, 2009.

Fan, Q. Z., Zhang, Y., Ma, W. C., Ma, H. X., Feng, J. L., Yu, Q., Yang, X., Ng, S. K. W., Fu, Q. Y., and Chen, L. M.: Spatial and Seasonal Dynamics of Ship Emissions over the Yangtze River Delta and East China Sea and Their Potential Environmental Influence, Environmental Science & Technology, 50, 1322-1329, 10.1021/acs.est.5b03965, 2016.

Feng, X., Mao, R., Gong, D.-Y., Zhao, C., Wu, C., Zhao, C., Wu, G., Lin, Z., Liu, X., Wang, K., and Sun, Y.: Increased Dust Aerosols in the High Troposphere Over the Tibetan Plateau From 1990s to 2000s, Journal of Geophysical Research: Atmospheres, 125, e2020JD032807, https://doi.org/10.1029/2020JD032807, 2020.

Ge, X. L., He, Y. A., Sun, Y. L., Xu, J. Z., Wang, J. F., Shen, Y. F., and Chen, M. D.: Characteristics and Formation Mechanisms of Fine Particulate Nitrate in Typical Urban Areas in China, Atmosphere, 8, 12, 10.3390/atmos8030062, 2017.

Ginoux, P., Prospero, J. M., Torres, O., and Chin, M.: Long-term simulation of global dust distribution with the GOCART model: correlation with North Atlantic Oscillation, Environmental Modelling & Software, 19, 113-128, https://doi.org/10.1016/S1364-8152(03)00114-2, 2004.

Goodman, M. M., Carling, G. T., Fernandez, D. P., Rey, K. A., Hale, C. A., Bickmore, B. R., Nelson, S. T., and Munroe, J. S.: Trace element chemistry of atmospheric deposition along the Wasatch Front (Utah, USA) reflects regional playa dust and local urban aerosols, Chemical Geology, 530, 10.1016/j.chemgeo.2019.119317, 2019.

Hammond, D. M., Dvonch, J. T., Keeler, G. J., Parker, E. A., Kamal, A. S., Barres, J. A., Yip, F. Y., and Brakefield-Caldwell, W.: Sources of ambient fine particulate matter at two

731 community sites in Detroit, Michigan, Atmos. Environ., 42, 720-732,
732 10.1016/j.atmosenv.2007.09.065, 2008.
733 Hertel, O., Skjoth, C. A., Reis, S., Bleeker, A., Harrison, R. M., Cape, J. N., Fowler, D.,
734 Skiba, U., Simpson, D., Jickells, T., Kulmala, M., Gyldenkaerne, S., Sorensen, L. L., Erisman,
735 J. W., and Sutton, M. A.: Governing processes for reactive nitrogen compounds in the European
736 atmosphere, Biogeosciences, 9, 4921-4954, 10.5194/bg-9-4921-2012, 2012.
737 Hilario, M. R. A., Cruz, M. T., Cambaliza, M. O. L., Reid, J. S., Xian, P., Simpas, J. B.,
738 Lagrosas, N. D., Uy, S. N. Y., Cliff, S., and Zhao, Y. J.: Investigating size-segregated sources
739 of elemental composition of particulate matter in the South China Sea during the 2011 Vasco
740 cruise, Atmospheric Chemistry And Physics, 20, 1255-1276, 10.5194/acp-20-1255-2020, 2020.
741 Hsu, S.-C., Lee, C. S. L., Huh, C.-A., Shaheen, R., Lin, F.-J., Liu, S. C., Liang, M.-C., and
742 Tao, J.: Ammonium deficiency caused by heterogeneous reactions during a super Asian dust
743 episode, Journal of Geophysical Research: Atmospheres, 119, 6803-6817,
744 10.1002/2013jd021096, 2014.
745 Huang, K., Fu, J. S., Lin, N.-H., Wang, S.-H., Dong, X., and Wang, G.: Superposition of
746 Gobi Dust and Southeast Asian Biomass Burning: The Effect of Multisource Long-Range
747 Transport on Aerosol Optical Properties and Regional Meteorology Modification, Journal of
748 Geophysical Research: Atmospheres, 124, 9464-9483, https://doi.org/10.1029/2018JD030241,
749 2019.
750 Huang, K., Zhuang, G., Li, J., Wang, Q., Sun, Y., Lin, Y., and Fu, J. S.: Mixing of Asian
751 dust with pollution aerosol and the transformation of aerosol components during the dust storm
752 over China in spring 2007, Journal of Geophysical Research, 115, 10.1029/2009jd013145,
753 2010a.
754 Huang, K., Zhuang, G. S., Li, J. A., Wang, Q. Z., Sun, Y. L., Lin, Y. F., and Fu, J. S.: Mixing
755 of Asian dust with pollution aerosol and the transformation of aerosol components during the
756 dust storm over China in spring 2007, J Geophys Res-Atmos, 115, Artn D00k13
757 10.1029/2009jd013145, 2010b.
758 Huang, X., Ding, A. J., Gao, J., Zheng, B., Zhou, D. R., Qi, X. M., Tang, R., Wang, J. P.,
759 Ren, C. H., Nie, W., Chi, X. G., Xu, Z., Chen, L. D., Li, Y. Y., Che, F., Pang, N. N., Wang, H.
760 K., Tong, D., Qin, W., Cheng, W., Liu, W. J., Fu, Q. Y., Liu, B. X., Chai, F. H., Davis, S. J.,
761 Zhang, Q., and He, K. B.: Enhanced secondary pollution offset reduction of primary emissions
762 during COVID-19 lockdown in China, Natl Sci Rev, 8, ARTN nwaa137
763 10.1093/nsr/nwaa137, 2021.
764 Jeong, G. Y.: Bulk and single-particle mineralogy of Asian dust and a comparison with its
765 source soils, J Geophys Res-Atmos, 113, Artn D02208
766 10.1029/2007jd008606, 2008.

Ji, Y., Qin, X. F., Wang, B., Xu, J., Shen, J. D., Chen, J. M., Huang, K., Deng, C. R., Yan, R. C., Xu, K. E., and Zhang, T.: Counteractive effects of regional transport and emission control on the formation of fine particles: a case study during the Hangzhou G20 summit, Atmos Chem Phys, 18, 13581-13600, 10.5194/acp-18-13581-2018, 2018.

Jiang, Y., Zhuang, G., Wang, Q., Huang, K., Deng, C., Yu, G., Xu, C., Fu, Q., Lin, Y., Fu, J. S., Li, M., and Zhou, Z.: Impact of mixed anthropogenic and natural emissions on air quality and eco-environment—the major water-soluble components in aerosols from northwest to offshore isle, Air Quality, Atmosphere & Health, 11, 521-534, 10.1007/s11869-018-0557-5, 2018.

Laskin, A., Wietsma, T. W., Krueger, B. J., and Grassian, V. H.: Heterogeneous chemistry of individual mineral dust particles with nitric acid: A combined CCSEM/EDX, ESEM, and ICP-MS study, J Geophys Res-Atmos, 110, Artn D10208

10.1029/2004jd005206, 2005.

Li, T., Wang, Y., Zhou, J., Wang, T., Ding, A. J., Nie, W., Xue, L. K., Wang, X. F., and Wang, W. X.: Evolution of trace elements in the planetary boundary layer in southern China: Effects of dust storms and aerosol-cloud interactions, J Geophys Res-Atmos, 122, 3492-3506, 10.1002/2016jd025541, 2017.

Liang, Y., Liu, Y., Wang, H., Li, L., Duan, Y., and Lu, K.: Regional characteristics of ground-level ozone in Shanghai based on PCA analysis, Acta Scientiae Circumstantiae, 38, 3807-3815, 2018.

Liu, H., Liu, S., Xue, B., Lv, Z., Meng, Z., Yang, X., Xue, T., Yu, Q., and He, K.: Ground-level ozone pollution and its health impacts in China, Atmospheric Environment, 173, 223-230, https://doi.org/10.1016/j.atmosenv.2017.11.014, 2018.

Liu, J., Ding, J., Rexiding, M., Li, X., Zhang, J., Ran, S., Bao, Q., and Ge, X.: Characteristics of dust aerosols and identification of dust sources in Xinjiang, China, Atmospheric Environment, 262, 118651, https://doi.org/10.1016/j.atmosenv.2021.118651, 2021.

Liu, Y. C., Zhan, J. L., Zheng, F. X., Song, B. Y., Zhang, Y. S., Ma, W., Hua, C. J., Xie, J. L., Bao, X. L., Yan, C., Bianchi, F., Petaja, T., Ding, A. J., Song, Y., He, H., and Kulmala, M.: Dust emission reduction enhanced gas-to-particle conversion of ammonia in the North China Plain, Nat Commun, 13, ARTN 6887

10.1038/s41467-022-34733-4, 2022.

Ma, S. Q., Zhang, X. L., Gao, C., Tong, Q. S., Xiu, A. J., Zhao, H. M., and Zhang, S. C.: Simulating Performance of CHIMERE on a Late Autumnal Dust Storm over Northern China, Sustainability-Basel, 11, ARTN 1074

10.3390/su11041074, 2019.

Malm, W. C., Sisler, J. F., Huffman, D., Eldred, R. A., and Cahill, T. A.: Spatial and seasonal trends in particle concentration and optical extinction in the United States, Journal of Geophysical Research: Atmospheres, 99, 1347-1370, https://doi.org/10.1029/93JD02916, 1994.

Mentel, T. F., Bleilebens, D., and Wahner, A.: A study of nighttime nitrogen oxide oxidation in a large reaction chamber—the fate of NO2, N2O5, HNO3, and O3 at different humidities, Atmospheric Environment, 30, 4007-4020, https://doi.org/10.1016/1352-2310(96)00117-3, 1996.

Nagashima, K., Suzuki, Y., Irino, T., Nakagawa, T., Tada, R., Hara, Y., Yamada, K., and Kurosaki, Y.: Asian dust transport during the last century recorded in Lake Suigetsu sediments, Geophysical Research Letters, 43, 2835-2842, https://doi.org/10.1002/2015GL067589, 2016.

Nenes, A., Pandis, S. N., and Pilinis, C.: ISORROPIA: A new thermodynamic equilibrium model for multiphase multicomponent inorganic aerosols, Aquat. Geochem., 4, 123-152, 10.1023/a:1009604003981, 1998.

Patel, A. and Rastogi, N.: Chemical Composition and Oxidative Potential of Atmospheric PM10 over the Arabian Sea, ACS Earth Space Chem., 4, 112-121, 10.1021/acsearthspacechem.9b00285, 2020.

Perez, N., Pey, J., Reche, C., Cortes, J., Alastuey, A., and Querol, X.: Impact of harbour emissions on ambient PM10 and PM2.5 in Barcelona (Spain): Evidences of secondary aerosol formation within the urban area, Science Of the Total Environment, 571, 237-250, 10.1016/j.scitotenv.2016.07.025, 2016.

Petetin, H., Sciare, J., Bressi, M., Gros, V., Rosso, A., Sanchez, O., Sarda-Estève, R., Petit, J. E., and Beekmann, M.: Assessing the ammonium nitrate formation regime in the Paris megacity and its representation in the CHIMERE model, Atmos. Chem. Phys., 16, 10419-10440, 10.5194/acp-16-10419-2016, 2016.

Shen, L., Zhao, C., Ma, Z., Li, Z., Li, J., and Wang, K.: Observed decrease of summer sea-land breeze in Shanghai from 1994 to 2014 and its association with urbanization, Atmospheric Research, 227, 198-209, https://doi.org/10.1016/j.atmosres.2019.05.007, 2019.

Song, S., Gao, M., Xu, W., Shao, J., Shi, G., Wang, S., Wang, Y., Sun, Y., and McElroy, M. B.: Fine-particle pH for Beijing winter haze as inferred from different thermodynamic equilibrium models, Atmos. Chem. Phys., 18, 7423-7438, 10.5194/acp-18-7423-2018, 2018.

Su, L., Yuan, Z., Fung, J. C. H., and Lau, A. K. H.: A comparison of HYSPLIT backward trajectories generated from two GDAS datasets, Science of The Total Environment, 506-507, 527-537, https://doi.org/10.1016/j.scitotenv.2014.11.072, 2015.

Sun, P., Nie, W., Wang, T., Chi, X., Huang, X., Xu, Z., Zhu, C., Wang, L., Qi, X., Zhang, Q., and Ding, A.: Impact of air transport and secondary formation on haze pollution in the Yangtze River Delta: In situ online observations in Shanghai and Nanjing, Atmospheric

Environment, 225, 117350, https://doi.org/10.1016/j.atmosenv.2020.117350, 2020.

Tang, M., Cziczo, D. J., and Grassian, V. H.: Interactions of Water with Mineral Dust Aerosol: Water Adsorption, Hygroscopicity, Cloud Condensation, and Ice Nucleation, Chemical Reviews, 116, 4205-4259, 10.1021/acs.chemrev.5b00529, 2016.

Tang, M. J., Huang, X., Lu, K. D., Ge, M. F., Li, Y. J., Cheng, P., Zhu, T., Ding, A. J., Zhang, Y. H., Gligorovski, S., Song, W., Ding, X., Bi, X. H., and Wang, X. M.: Heterogeneous reactions of mineral dust aerosol: implications for tropospheric oxidation capacity, Atmos Chem Phys, 17, 11727-11777, 10.5194/acp-17-11727-2017, 2017.

Tian, R., Ma, X., Sha, T., Pan, X., and Wang, Z.: Exploring dust heterogeneous chemistry over China: Insights from field observation and GEOS-Chem simulation, Science of The Total Environment, 798, 149307, https://doi.org/10.1016/j.scitotenv.2021.149307, 2021.

Vicars, W. C. and Sickman, J. O.: Mineral dust transport to the Sierra Nevada, California: Loading rates and potential source areas, Journal of Geophysical Research, 116, 10.1029/2010jg001394, 2011.

Wang, G., Chen, J., Xu, J., Yun, L., Zhang, M., Li, H., Qin, X., Deng, C., Zheng, H., Gui, H., Liu, J., and Huang, K.: Atmospheric processing at the sea-land interface over the South China Sea: secondary aerosol formation, aerosol acidity, and role of sea salts, Journal of Geophysical Research: Atmospheres, n/a, e2021JD036255, https://doi.org/10.1029/2021JD036255,

Wang, G. C., Chen, J., Xu, J., Yun, L., Zhang, M. D., Li, H., Qin, X. F., Deng, C. R., Zheng, H. T., Gui, H. Q., Liu, J. G., and Huang, K.: Atmospheric Processing at the Sea-Land Interface Over the South China Sea: Secondary Aerosol Formation, Aerosol Acidity, and Role of Sea Salts, J. Geophys. Res.-Atmos., 127, 10.1029/2021jd036255, 2022a.

Wang, G. H., Cheng, C. L., Huang, Y., Tao, J., Ren, Y. Q., Wu, F., Meng, J. J., Li, J. J., Cheng, Y. T., Cao, J. J., Liu, S. X., Zhang, T., Zhang, R., and Chen, Y. B.: Evolution of aerosol chemistry in Xi'an, inland China, during the dust storm period of 2013-Part 1: Sources, chemical forms and formation mechanisms of nitrate and sulfate, Atmospheric Chemistry And Physics, 14, 11571-11585, 10.5194/acp-14-11571-2014, 2014.

Wang, H. C. and Lu, K. D.: Determination and Parameterization of the Heterogeneous Uptake Coefficient of Dinitrogen Pentoxide (N2O5), Prog Chem, 28, 917-933, 10.7536/Pc151225, 2016.

Wang, J. J., Zhang, M. G., Bai, X. L., Tan, H. J., Li, S., Liu, J. P., Zhang, R., Wolters, M. A., Qin, X. Y., Zhang, M. M., Lin, H. M., Li, Y. N., Li, J., and Chen, L. Q.: Large-scale transport of PM2.5 in the lower troposphere during winter cold surges in China, Sci Rep, 7, 10, 10.1038/s41598-017-13217-2, 2017.

Wang, L., Du, H., Chen, J., Zhang, M., Huang, X., Tan, H., Kong, L., and Geng, F.:

875 Consecutive transport of anthropogenic air masses and dust storm plume: Two case events at
876 Shanghai, China, Atmospheric Research, 127, 22-33,
877 https://doi.org/10.1016/j.atmosres.2013.02.011, 2013.
878 Wang, N., Zheng, P., Wang, R., Wei, B., An, Z., Li, M., Xie, J., Wang, Z., Wang, H., and
879 He, M.: Homogeneous and heterogeneous atmospheric ozonolysis of acrylonitrile on the
880 mineral dust aerosols surface, Journal of Environmental Chemical Engineering, 9, 106654,
881 https://doi.org/10.1016/j.jece.2021.106654, 2021.
882 Wang, Q., Wang, X., Huang, R., Wu, J., Xiao, Y., Hu, M., Fu, Q., Duan, Y., and Chen, J.-
883 M.: Regional Transport of PM 2.5 and O 3 Based on Complex Network Method and Chemical
884 Transport Model in the Yangtze River Delta, China, Journal of Geophysical Research:
885 Atmospheres, 127, 10.1029/2021JD034807, 2022b.
886 Wang, Z., Pan, X. L., Uno, I., Chen, X. S., Yamamoto, S., Zheng, H. T., Li, J., and Wang,
887 Z. F.: Importance of mineral dust and anthropogenic pollutants mixing during a long-lasting
888 high PM event over East Asia, Environ. Pollut., 234, 368-378, 10.1016/j.envpol.2017.11.068,
889 2018.
890 Wang, Z. L., Huang, X., Wang, N., Xu, J. W., and Ding, A. J.: Aerosol-Radiation
891 Interactions of Dust Storm Deteriorate Particle and Ozone Pollution in East China, J Geophys
892 Res-Atmos, 125, ARTN e2020JD033601
893 10.1029/2020JD033601, 2020.
894 West, J. J., Ansari, A. S., and Pandis, S. N.: Marginal PM25: Nonlinear Aerosol Mass
895 Response to Sulfate Reductions in the Eastern United States, Journal of the Air & Waste
896 Management Association, 49, 1415-1424, 10.1080/10473289.1999.10463973, 1999.
897 Wu, C., Zhang, S., Wang, G., Lv, S., Li, D., Liu, L., Li, J., Liu, S., Du, W., Meng, J., Qiao,
898 L., Zhou, M., Huang, C., and Wang, H.: Efficient Heterogeneous Formation of Ammonium
899 Nitrate on the Saline Mineral Particle Surface in the Atmosphere of East Asia during Dust Storm
900 Periods, Environmental Science & Technology, 54, 15622-15630, 10.1021/acs.est.0c04544,
901 2020.
902 Wu, F., Cheng, Y., Hu, T. F., Song, N., Zhang, F., Shi, Z. B., Ho, S. S. H., Cao, J. J., and
903 Zhang, D. Z.: Saltation-Sandblasting Processes Driving Enrichment of Water- Soluble Salts in
904 Mineral Dust, Environ Sci Tech Let, 9, 921-928, 10.1021/acs.estlett.2c00652, 2022.
905 Xie, S. D., Yu, T., Zhang, Y. H., Zeng, L. M., Qi, L., and Tang, X. Y.: Characteristics of
906 PM10, SO2, NO, and O-3 in ambient air during the dust storm period in Beijing, Sci Total
907 Environ, 345, 153-164, 10.1016/j.scitotenv.2004.10.013, 2005.
908 Xu, J., Chen, J., Zhao, N., Wang, G. C., Yu, G. Y., Li, H., Huo, J. T., Lin, Y. F., Fu, Q. Y.,
909 Guo, H. Y., Deng, C. R., Lee, S. H., Chen, J. M., and Huang, K.: Importance of gas-particle
910 partitioning of ammonia in haze formation in the rural agricultural environment, Atmospheric

911 Chemistry and Physics, 20, 7259-7269, 10.5194/acp-20-7259-2020, 2020.
912 Xu, P., Zhang, J. K., Ji, D. S., Liu, Z. R., Tang, G. Q., Hu, B., Jiang, C. S., and Wang, Y.
913 S.: Evaluating the Effects of Springtime Dust Storms over Beijing and the Associated
914 Characteristics of Sub-Micron Aerosol, Aerosol Air Qual Res, 17, 680-692,
915 10.4209/aaqr.2016.05.0195, 2017.
916 Yang, Y., Wang, Z. L., Lou, S. J., Xue, L., Lu, J. P., Wang, H. Y., Wang, J. D., Ding, A. J.,
917 and Huang, X.: Strong ozone intrusions associated with super dust storms in East Asia, Atmos
918 Environ, 290, ARTN 119355
919 10.1016/j.atmosenv.2022.119355, 2022.
920 Yu, S. C., Dennis, R., Roselle, S., Nenes, A., Walker, J., Eder, B., Schere, K., Swall, J., and
921 Robarge, W.: An assessment of the ability of three-dimensional air quality models with current
922 thermodynamic equilibrium models to predict aerosol NO3, J. Geophys. Res.-Atmos., 110,
923 10.1029/2004jd004718, 2005.
924 Zhang, D., Iwasaka, Y., Shi, G., Zang, J., Hu, M., and Li, C.: Separated status of the natural
925 dust plume and polluted air masses in an Asian dust storm event at coastal areas of China,
926 Journal of Geophysical Research (Atmospheres), 110, D06302, 10.1029/2004jd005305, 2005.
927 Zhang, S. P., Xing, J., Sarwar, G., Ge, Y. L., He, H., Duan, F. K., Zhao, Y., He, K. B., Zhu,
928 L. D., and Chu, B. W.: Parameterization of heterogeneous reaction of SO2 to sulfate on dust
929 with coexistence of NH3 and NO2 under different humidity conditions, Atmos Environ, 208,
930 133-140, 10.1016/j.atmosenv.2019.04.004, 2019.
931 Zhang, X. L., Wu, G. J., Zhang, C. L., Xu, T. L., and Zhou, Q. Q.: What is the real role of
932 iron oxides in the optical properties of dust aerosols?, Atmos Chem Phys, 15, 12159-12177,
933 10.5194/acp-15-12159-2015, 2015.
934 Zhao, D., Xin, J., Wang, W., Jia, D., Wang, Z., Xiao, H., Liu, C., Zhou, J., Tong, L., Ma,
935 Y., Wen, T.-X., Wu, F.-K., and Wang, L.: Effects of the sea-land breeze on coastal ozone
936 pollution in the Yangtze River Delta, Science of The Total Environment, 807,
937 10.1016/j.scitotenv.2021.150306, 2021.
938 Zheng, G. J., Duan, F. K., Su, H., Ma, Y. L., Cheng, Y., Zheng, B., Zhang, Q., Huang, T.,
939 Kimoto, T., Chang, D., Poschl, U., Cheng, Y. F., and He, K. B.: Exploring the severe winter
940 haze in Beijing: the impact of synoptic weather, regional transport and heterogeneous reactions,
941 Atmos Chem Phys, 15, 2969-2983, 10.5194/acp-15-2969-2015, 2015.
942 Zheng, Y., Zhao, T., Che, H., Liu, Y., Han, Y., Liu, C., Xiong, J., Liu, J., and Zhou, Y.: A
943 20-year simulated climatology of global dust aerosol deposition, Science of The Total
944 Environment, 557-558, 861-868, https://doi.org/10.1016/j.scitotenv.2016.03.086, 2016.
945